SqUNet: An High-Performance Network for Crater Detection With DEM Data

Yaqi Zhao and Hongxia Ye, *Senior Member, IEEE*

Abstract—**Identification of craters plays an essential role in planetary exploration. This article proposes a new neural network, called Square U-Net (SqUNet) for automatic detection of craters using digital elevation model (DEM) images of lunar and Mars. The SqUNet uses an embedded U-Net architecture, which includes an encoding and a decoding structure, to replace the traditional convolution module. This kind of structure can significantly improve the feature learning ability. Moreover, a skip link is added inside the embedded U-Net structure to retain the feature information of the original map. We compare our SqUNet model with six other state-of-the-art crater detection models through experiments. The experiments show that the SqUNet can effectively improve the recall rate and the precision of detection. Our model can not only discover new craters but also improve the accuracy of crater segmentation. In addition, the testing results on the Mars DEM dataset have also demonstrated the strong generalization and robustness of the SqUNet network model. It holds significant potential for various applications, providing valuable support for lunar exploration and geological research.**

Index Terms—**Crater detection, deep learning, planetary exploration, U-Net.**

I. INTRODUCTION

LUNAR craters are the dominant features on the lunar surface, and provide essential information about lunar morphology and its evolution. The distribution of craters provides valuable clues to reveal the aging process of geological structures [1], and is also one of the important factors for landing-site selection of lunar probes [2], [3], [4]. The traditional methods [1], [5] rely on planetary scientists to manually mark the craters one by one on the remote sensing images of the lunar surface, which is very time-consuming and labor-intensive. It is also challenging to cover all areas of the lunar surface. Therefore, a high-performance and high-precision method for automatic detection of craters is very necessary.

Currently, some automatic detection methods for lunar craters was developed. These methods can be divided into two categories: 1) Methods based on the optical images, such as Hough transform [6], genetic algorithm [7], pattern recognition [8], and other methods. 2) Methods based on the digital elevation

model (DEM) images, such as machine learning methods [10], morphological methods [11], and convolutional neural networks [12], [13]. Since the optical images are easier to obtain and have higher resolution than DEM images, most crater detection methods are based on optical images. However, optical images is often disturbed by unconstrained factors such as solar illumination, while the complexity of the terrain on the planetary surface increases the degree of lighting interference. As a result, this further complicates the detection of impact craters [9]. However, the appearance of craters in DEM images is not affected by the direction of incoming sunlight, which makes it easier to train the model for crater detection. This article will use the DEM images to detect lunar craters.

With the popularity of computer vision, deep learning has been widely used in crater detection tasks. Deep learning algorithms based on convolutional neural networks (CNNs) have achieved great success in both the segmentation and detection tasks of remote sensing images [14], [15]. For example, Long et al. [16] introduced the fully convolutional neural network (FCN) to solve the pixel-level segmentation problem to perform end-to-end image segmentation tasks, which was superior to other algorithms at that time. The FCN uses the upsampling deconvolution method to restore the pixel-level output feature map. Ronneberger et al. [17] proposed a classical encoder-decoder network U-Net, which consists of an encoder path to capture the high-level semantic features and a corresponding decoder path to achieve the accurate restoration of segmentation targets. The skip connections between layers can improve the segmentation performance of the images and overcome the problems of gradient disappearance and network degradation.

In recent years, there have been numerous advancements in the field of target segmentation networks. The DeepLabv3+ proposed by Chen et al. [18] has solved many problems that traditional image segmentation methods face, such as edge aliasing, noise, and rough segmentation results. In addition, due to its high efficiency and high accuracy, DeepLabv3+ can be applied to many computer vision tasks, such as object detection, scene understanding, and autonomous driving. Some researchers have also applied DeepLabv3+ to medical image segmentation tasks, achieving good results. Li et al. [19] proposed the A2-FPN model, which utilizes multiscale feature extraction and adaptive pooling operations for semantic segmentation of high-resolution remote sensing images, to achieve more accurate classification results. Chen et al. [20] proposed a novel medical image segmentation model called TransUNet, which combines the advantages of Transformer and UNet and exhibits better performance and

The authors are with the Key Laboratory for Information Science of Electromagnetic Waves (MoE), Fudan University, Shanghai 200433, China (e-mail: yqzhao21@m.fudan.edu.cn; yehongxia@fudan.edu.cn).

generalization ability. TransUNet provides important references and inspirations for the research and application in the field of medical image segmentation. Swin-UNet proposed by Cao et al. [21] is a semantic segmentation model based on Swin Transformer. It combines the advantages of both UNet and Swin Transformer [22], and processes feature maps in a hierarchical manner, significantly reducing computational complexity and the number of parameters while improving segmentation efficiency. Swin-UNet has achieved excellent segmentation results on multiple public datasets. These network models have overcome limitations of traditional methods and achieved remarkable performance and wide-ranging applications. However, these models have not yet been applied to the segmentation of lunar craters. We will further explore their effectiveness within the context of lunar crater analysis.

In addition to the aforementioned advanced target witnessed the emergence of several competitive network models. These models have made significant contributions to the domain of lunar crater segmentation, providing our innovation with new perspectives and avenues to explore. Silburt et al. [12] trained a CNN architecture that included a U-Net model for edge segmentation and a template matching algorithm for crater extraction. They successfully discovered about 45% of new craters in the test dataset of lunar DEM images. The model was also migrated to detect the impact craters on the Mercury surface and correctly identify about 70% of craters. However, the U-Net network layers they used are relatively shallow, resulting in insufficient learning ability for feature maps and poor segmentation ability for crater contours. Lee [23] used the U-Net model trained on the lunar DEM images by Silburt to test the DEM images of Mars, and achieved a recall rate of 67% and a precision of 78%. To improve the recall and precision of crater identification, Wang et al. [24] proposed a new CNN structure based on U-Net, called Effective Residual U-Net (ERU-Net), which uses the residual convolution blocks instead of traditional convolutional blocks. Their model achieved 81.2% recall and 75.4% precision for crater identification on the training dataset of 30 000 DEM images of the lunar surface. Mao et al. [25] combined a complementary strategy with the U-Net detecting lunar impact craters. Their work underscores the merits of integrating multiple techniques and data sources, showcasing the potential of this approach in augmenting the accuracy and reliability of lunar crater detection tasks. Jia et al. [26] proposed an automated algorithm named Nested Attention-Aware U-Net (NAU-Net) based on UNet++ architecture and attention networks for the detection of lunar impact craters. Their network employs nested intensive attention-aware connections and profound supervision, achieving 79.1% recall and 85.6% precision on the lunar DEM image dataset. Wu et al. [27] proposed a simplified full-scale skip connected UNet termed SUNet3+ to achieve fast and accurate crater detection on Mars surface with DEM data. The proposed architecture achieved a recall rate of 82.2% and an accuracy of 84.9%.

The aforementioned algorithms for lunar crater detection made some minor modifications to U-Net architecture, such as adding extra convolutional layers or utilizing pretrained encoders. These modifications have get relatively good segmentation output for lunar crater detection. However, they still fail to effectively capture the complex features of the craters, and the precision and performance is still limited.

To improve the recall and precision of crater detection, we explore a new embedded U-Net structure, called Square U-Net (SqUNet), which uses an embedded U-Net architecture instead of the traditional convolution module. The encoding structure and decoding structure are used in each embedded U-Net structure, to greatly enhance the capability of extracting multilevel features. At the same time, a skip link is added in the output part to retain the original feature map information. The main contributions of this article are as follows.

1) A high-performance crater detection network—SqUNet. SqUNet uses an encoding and decoding structure instead of the traditional convolution module, which enables the network to refine features at different levels, so that the recall and precision of lunar impact crater detection is significantly improved.
2) We developed an efficient workflow for end-to-end crater detection on DEM data.
3) We validated the effectiveness of the U-Net module through ablation studies.
4) The high performance of SqUNet is verified by comparing with six other state-of-the-art algorithms. The experimental results showed that SqUNet had the highest recall (87.5%) and precision (80.7%), and the smallest error for identifying lunar craters.
5) We showed generalization of SqUNet to Martian crater detection, proving its applicability to other planetary bodies.

The rest of this article is organized as follows. In Section II, we describe the methodology, including data pre-processing methods, network structure, and crater extraction algorithms in detail. In Section III, we conducted experimental comparisons between SqUNet and other state-of-the-art semantic segmentation algorithms. We also compared SqUNet with several advanced algorithms specifically designed for crater detection. Furthermore, validation experiments were performed on the Mars dataset to evaluate the performance of SqUNet. Section IV provides some discussion and analysis. Finally, Section V concludes this article.

II. METHODOLOGY

A. Data Preparation

In this work, the downsampled DEM image is from the lunar Orbiter Laser Altimeter on the lunar Reconstruction Orbiter (LRO) and the Terrain Camera on SELENE lunar Orbiter. The latitude range is -60–60 degrees, and the longitude range is 0–360°. This DEM (see Fig. 1) is a PlateCarree projection with 92160×30720 pixels and a resolution of 118 m/pix (256 pixels/ degree) [28].

We use two existing publicly available crater catalog datasets. The first one is the global craters dataset with diameter larger than 20 km labeled by Head et al. [1]. The second one comes from the global crater dataset with diameter of 5–20 km, provided by Povilaitis et al. [5]. Both catalogs have relatively strict or conservative artificial labels for craters. Each catalog contains the longitude and latitude of the craters as well as their diameter size. We combine the two datasets and call the combined catalog
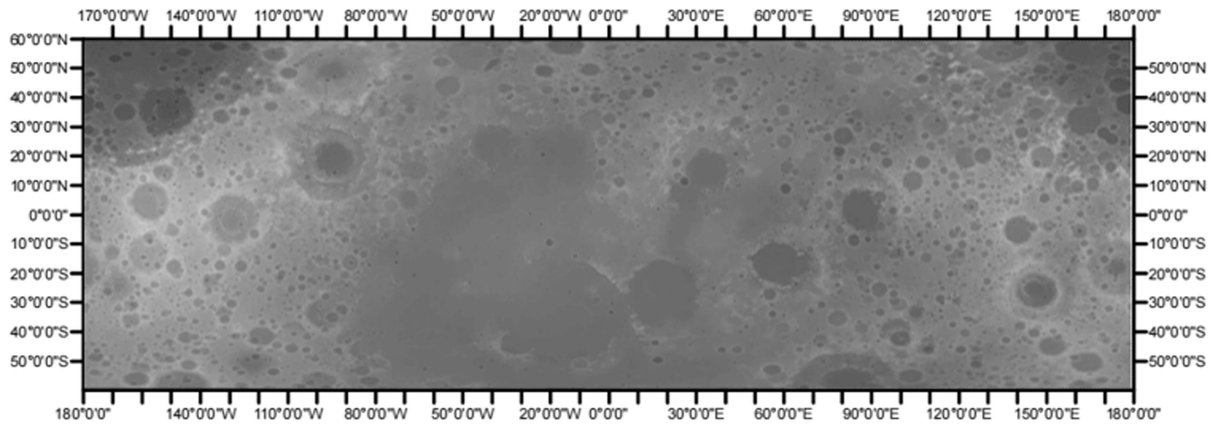
Fig. 1. DEM in the longitude range [−60°, 60°] and latitude range [−180°, 180°] for the lunar image.

TABLE I
DATASET OF LUNAR CRATERS

Source	Number of Craters	Diameter range
Head	4301	>20(km)
Povilaitis	19,335	5-20(km)

Fig. 2. Cartopy processed pictures and the label maps.

Head-LROC [29]. The crater statistics of the two datasets are shown in Table I.

We randomly crop the merged images (catalog Head-LROC) into square regions with minimum of 500 pixels (59 km) and maximum boundaries of 6500 pixels (770 km), We downsampled these images to 256 × 256 pixels to fit the network input size. Then, the Cartopy Python package [30] is used to convert these images to an orthographic projection to avoid noncircular craters at high latitudes due to image distortion. Here, Orthographic projection treats the moon as a sphere and gradually unfolds it from a single point to generate a map. In the process of the orthographic projection conversion, the original image often will become a nonsquare image. So we fill some zeros on the boundary to make it a square image, such as the black bars on the left images in Fig. 2. Finally a one-pixel-wide circle marks the crater target in each corresponding label map. The radius and center coordinates come from the physical location and diameter of the craters in the Head-LROC directory. We focus on the craters with radius of 5–40 pixels, and the corresponding diameter is 2.304–23449.684 km.

With the abovementioned preparation, we randomly generated 30 000 training datasets, 3000 validation datasets, and 3000 test datasets. Each data set contains a cropped DEM image and a corresponding label image. The position and size information of the crater in the label image is also preserved.

B. SqUNet Network Structure

From the visual features of the crater data, it can be seen that crater images do not have very complex texture features like natural scene data. At the same time, crater detection is mainly aimed at distinguishin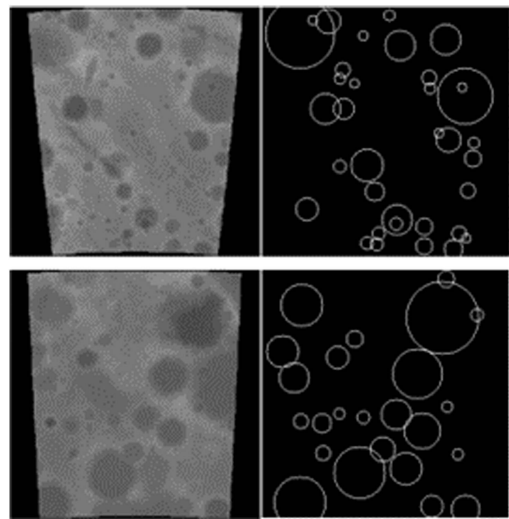g craters and background images, which is a typical binary classification recognition task. At present, U-Net [17] is widely used in the target recognition task of binary classification. Therefore, in the following crater detection task, we perform the crater recognition based on the U-Net network.

As shown in Fig. 3, the entire network architecture consists of an encoder (left) and a decoder (right), connected by multiple layers of skip connections. The encoder extracts and encodes features from the input image. These features contain the spatial information about objects in the input image. In the encoder part, we use a max pooling operation to downsample the output feature map of each unit. The pooling size is 2 × 2, and the feature map size is reduced to half of the original size. The decoder decodes the features obtained by the encoder into segmentation masks. It usually contains upsampling layers to upscale the feature maps to the same dimensions as the input image. In the decoder part, a 3 × 3 deconvolution with stride 2 is used as an upsampling layer to enlarge the size of the feature map.

In the U-Net network, the U-shaped encoding and decoding structure plays a role in feature optimization for image features. The multilevel feature maps of the encoder hold different levels
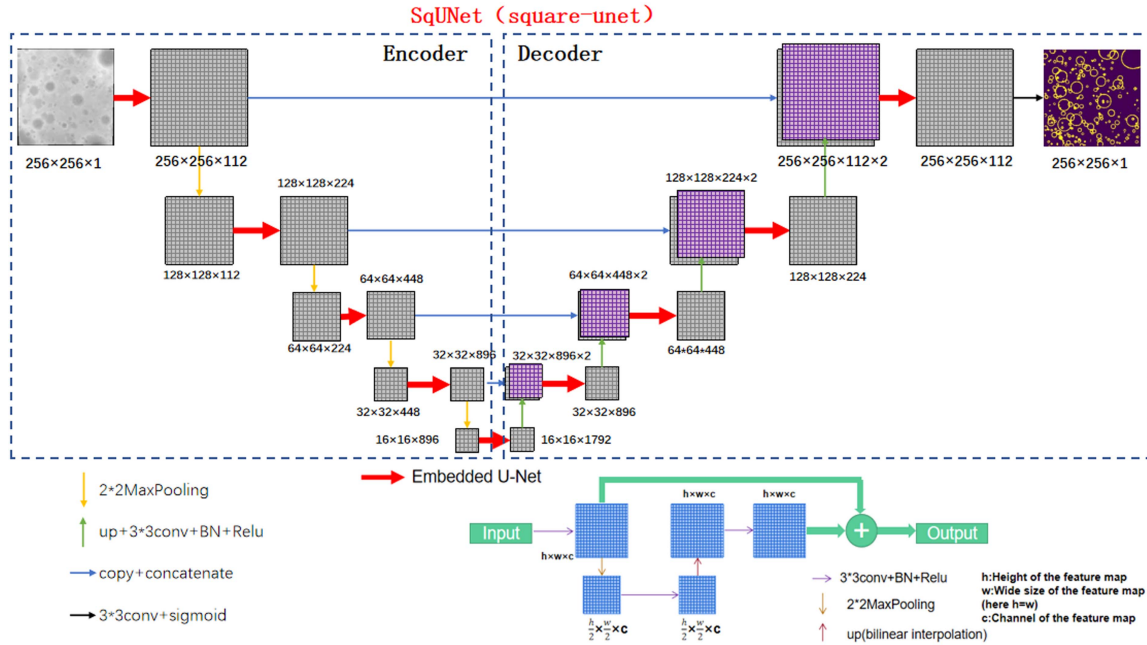
Fig. 3.　Network structure of SqUNet.

of feature information. Therefore, different levels of feature maps are used to extract and represent the contextual information at different levels of the image. Shallow feature maps typically contain lower-level features, such as crater rims. These shallow features can be used to learn about the shape of the crater. The deeper feature maps usually contain higher level features, such as the general information of craters, which can be used to identify and classify objects. For most semantic segmentation tasks, the encode–decode structures are commonly used to extract rich multiscale spatial information, thus, further improving the image segmentation effect. Therefore, in order to strengthen the role of the U-Net encoder–decoder structure in the model, we designed an embedded SqUNet structure based on the U-Net network. It uses U-Net as the network skeleton, and uses an embedded U-shaped encoding and decoding structure to replace the traditional convolution module, as shown in the red arrow in Fig. 3. The embedded U-Net, detailed in the low part of Fig. 3, uses the encoding and decoding structure in each convolution module to greatly optimize the learning ability.

Due to pooling calculations of the semantic segmentation model, it is usually difficult for low-resolution feature maps to fully restore the information of high-resolution feature maps through upsampling calculations. The introduction of skip connections plays a role in transferring feature maps and can optimize the convergence ability of the network. Therefore, in the embedded U-Net structure, we use the skip link to transfer the feature map of the encoding part to the decoding part, so that the original feature information of the crater image is supplemented, the original feature map of the crater can be restored to the greatest extent in the decoding part.

As shown in Fig. 3, each convolutional module is linked to an embedded U-Net structure, which contains three convolutional layers, a 2×2 maxpooling layer, and a 2×2 bilinear interpolation upsampling layer. Each convolutional layer has filters, and each filter uses a 3×3 padded convolution followed by the Rectified Linear Unit.

The network depth of the original U-Net is 5, and the number of initial filters is 64. The SqUNet network for lunar crater identification has a depth of 5 and an initial filter number of 112. After the last convolution operation is completed, the number of channels in the output feature map is adjusted to 1 through a 3×3 convolution layer, and then the output is activated by a sigmoid function to obtain the final output image.

C. Crater Extraction

Normalize a 256×256 pixel DEM image by subtracting the mean and dividing by the standard deviation for each channel, such that the output data follows a normal distribution with a mean of 0 and a standard deviation of 1. Then, input the normalized image into the SqUNet network for processing, a crater edge segmentation map with 256×256 pixels will be output, as shown in Fig. 4(c). Then, we will use the template matching algorithm of scikit-image [31] to extract the position and size of the crater from these segmented edges. The threshold 0.1 is set to get a binary predicted target output. The pixels with intensity greater than 0.1 are set to 1, and the rest are set to 0. With the matching threshold of P_m, rings with radius range of 5–40 pixels were iteratively generated using the scikit-image match-template algorithm. The rings larger than the matching threshold was classified as a crater. We evaluated various metrics on the test dataset when the matching thresholds $P_m = 0.3 \sim 0.8$, as shown in Table II. It can be seen that when P_m increases, the accuracy values increase, while the recall values decrease. When $P_m = 0.8$, a high precision of 96.2% is achieved, and the errors for Error_{la}, Error_{la}, and Error_r are
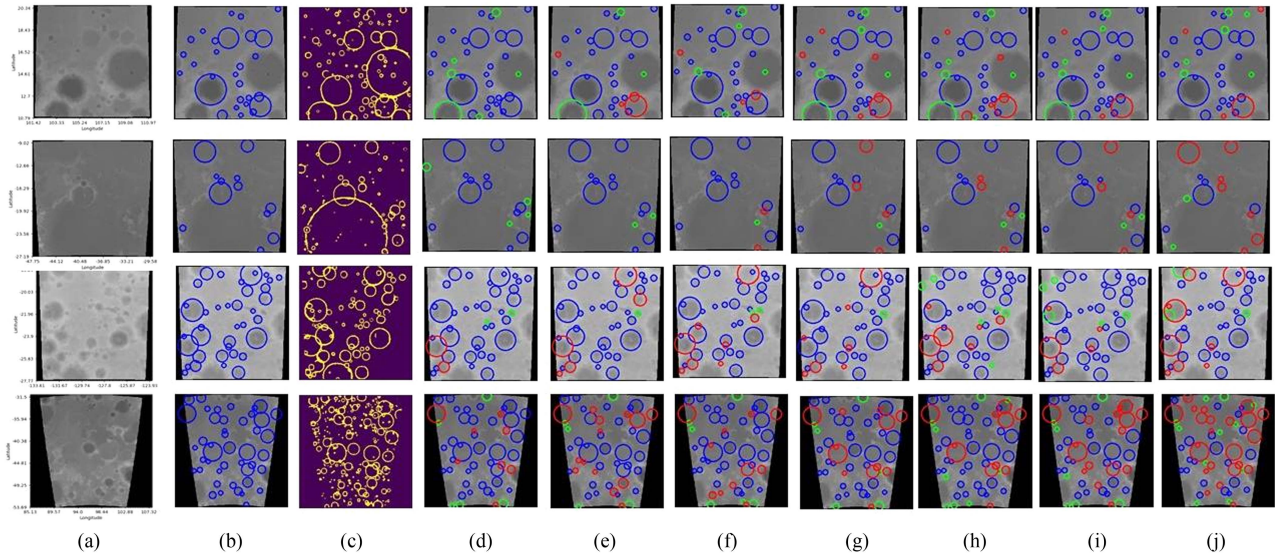
Fig. 4. Model performance comparision on test datasets. (a) Origin images. (b) Ground-truth labels from origin images. (c) Segmentation results from the SqUNet. (d) Detection results of SqUNet. (e)–(j) Detection results with other networks. (Red circles: Missed craters, blue circles: correctly identified craters, green circles: new craters).

TABLE II
RESULTS OF DIFFERENT PM ON THE TEST DATASETS

Metric	0.3	0.4	0.5	0.6	0.7	0.8
Recall	95.4%	93.4%	**87.5%**	72.8%	45.2%	15.9%
Precision	33.2%	60.1 %	80.7%	89.1%	92.9%	96.2%
F1-score	49.3%	73.1%	**82.8%**	80.1%	60.8%	27.3%
F2-score	69.4%	84.1%	**85.2%**	75.6%	50.4%	19.1%
$Error_{lo}$	13.5%	11.3%	8.9%	7.9%	7.6%	6.7%
$Error_{la}$	13.6%	11.9%	8.4%	8.2%	7.6%	6.2%
$Error_r$	10.4%	8.7%	6.8%	7.0%	6.6%	5.7%

The bold values indicate the superiority of the results of several evaluation indicators when $P_m = 0.5$.

the smallest. F1 provides a balance between precision and recall values. The optimal F1 score is 82.8% when $P_m = 0.5$, with precision at 80.7% and recall at 87.5%. The errors ($Error_{la}$, $Error_{la}$, and $Error_r$) are relatively small, with values of 8.9%, 8.4%, and 6.8%, respectively. F2 score emphasizes recall more, and the best F2 score of 85.2% is achieved when $P_m = 0.5$. Therefore, $P_m = 0.5$ is set in the following.

The extracted craters is recorded as (x_i, y_i, r_i), and the marked impact crater by experts is recorded as $(\hat{x}_j, \hat{y}_j, \hat{r}_j)$. The following limitation can obtain the optimal F1-score:

$$\left[(x_i - \hat{x}_j)^2 + (y_i - \hat{y}_j)^2\right] / [\min(r_i, \hat{r}_j)]^2 < D_{x,y} \quad (1)$$

$$\text{abs}(r_i - \hat{r}_j) / \min(r_i, \hat{r}_j) < D_r. \quad (2)$$

Here, $D_{x,y} = 1.8$ and $D_r = 1.0$ are hyperparameters [12].

III. EXPERIMENT

A. Experiment Set

This experiment is based on the PyTorch [32] framework. PyTorch is an open source machine learning framework. It is easy to debug, has automatic differentiation, and a big community. It is widely used in both academic research and industry applications. The hardware operating system is ubuntu, and an NVIDIA GeForce RTX 3090 graphics card is used for training. In model training, we use AdamW as the optimizer, the learning rate is 0.001, the weight_decay is 0.0001, and the loss function is set to cross-entropy loss. The number of iterations in the network is set to epoch 10 and the batch size is 3. During the experiment, we record and save the best model in the validation dataset, and use this model to evaluate on the test dataset.

B. Evaluate Metrics

Let P be the precision and R be the recall, which are calculated by Formulas

$$P = T_p / (T_p + F_p) \quad (3)$$

$$R = T_p / (T_p + F_n) \quad (4)$$

where T_p are true positives, representing the correctly identified craters (blue circles in the figure), F_p are false positives, representing the craters that do not match the real craters in the prediction result (green circles in the figure), and F_n are false negatives, representing missed craters (red circles in the figure). Recall tends to be generally lower when the precision is higher, and vice versa. To balance precision and recall, we use another parameter F-score (F_β), defined as

$$F_\beta = (1 + \beta^2) \times P \times R / (\beta^2 \times P + R). \quad (5)$$

TABLE III
ABLATION EXPERIMENTS ON EMBEDDED U-NET MODULE

Embedded U-Net	FPS	Recall	Precision	F1-score	F2-score
×	23.6	68.5%	75.8%	70.5%	68.9%
✓	25.3	**74.4%**	**76.2%**	**74.2%**	**74.1%**

The bold values indicate the superiority of the results of several evaluation indicators after adding the embedded U-Net modules.

Set to $\beta = 1$ when precision and Recall are equally important. The formula for F1 is as follows:

$$F_1 = 2 \times P \times R / (P + R). \tag{6}$$

In this experiment, a higher recall rate is more preferred because more craters are expected to be found, and $\beta = 2$ is set to obtain the F2 formula as follows:

$$F_2 = 5 \times P \times R / (4 \times P + R). \tag{7}$$

In addition to the essential evaluation indicators for crater identification, the accuracy of the location and size of craters is also an important indicator for evaluating models. The latitude error (Error_{la}), longitude error (Error_{lo}), and radius error (Error_r) of the identified craters are calculated by the following formulas:

$$\text{Error}_{lo} = \text{abs}\,(lo_p - lo_t) \times 2/\,(r_p + r_t) \tag{8}$$

$$\text{Error}_{la} = \text{abs}\,(la_p - la_t) \times 2/\,(r_p + r_t) \tag{9}$$

$$\text{Error}_r = \text{abs}\,(r_p - r_t) \times 2/\,(r_p + r_t) \tag{10}$$

where lo_p and lo_t are the longitude values of the predicted crater and the real crater, respectively. la_p and la_t are the latitude values of the predicted crater and the real crater, respectively. r_p and r_t are the radius values of the predicted crater and the real crater.

To evaluate the speed of crater detection using neural network, we introduced the concept of frames per second (FPS). FPS refers to the number of picture frames that the model processes per second and is used as a measure of time. A higher FPS value indicates that the model is capable of detecting more pictures per second, resulting in a faster detection speed. Therefore, FPS serves as an indicator to assess the speed of the model's detection.

C. Quantify Analysis and Visualize Results

We use lunar DEM images to generate a small dataset, which contains 3000 training datasets, 300 validation datasets, and 300 test datasets. To verify the performance of the embedded U-Net module, we train 5 iterations on the small dataset. Table III shows that the performance of detecting lunar craters has been significantly improved after adding the embedded U-Net modules, although the detection speed was slightly reduced. For example, the recall rate, f1 score, and f2 score increased by 5.9%, 3.7%, and 5.2%, respectively, which validates the effectiveness of the model.

We compared SqUNet with four other advanced target segmentation networks, including Swin-unet [21], Transunet [20], DeeplabV3+ [18], and A2-FPN [19]. The experimental results

TABLE IV
COMPARISON OF SQUNET AND OTHER SEGMENTATION MODELS

Metric	Swin-unet	Transunet	DeeplabV3+	A2FPN	SqUNet
Recall	44.6%	64.1%	56.4%	59.1%	77.8%
Precision	83.9%	77.9%	80.5%	78.3%	79.1%
F1-score	55.6%	68.5%	64.3%	67.4%	78.4%
F2-score	49.2%	66.5%	60.0%	62.1%	78.1%
$Error_{lo}$	9.5%	10.5%	11.2%	10.9%	9.3%
$Error_{la}$	10.4%	10.3%	10.2%	10.7%	9.9%
$Error_r$	8.0%	8.4%	8.3%	8.2%	7.9%
FPS	32.1	34.5	30.9	32.5	25.5

are shown in Table IV. The experimental results show that SqUNet has better overall performance than the other models, which confirms that the U-Net's encoder-decoder structure is more suitable for segmenting lunar craters.

We choose six other competing models for comparison, namely DeepMoon [12], ERU-Net [19], D-LinkNet [14], UNet++ [33], NAU-Net [26], and SUNet3+ [27]. These six network models are all relatively recent and competitive architectures in the field of crater detection. Each of these models has been meticulously designed and refined for the specific purpose of crater detection. We set the initial number of filters to 112 in this experiment, and all models use the same dataset (30 000 training datasets, 3 000 validation datasets, and 3 000 testing datasets). Quantitative analysis effectively demonstrates the effectiveness and robustness of the algorithm proposed in this article. The comparison results are shown in Table V. The experimental results show that the SqUNet proposed in this article has a significant improvement in the recall, and the improvement of F1-score and F2-score proves the high performance of the model. Compared with the other six models, SqUNet has smaller values on the three indicators of Error_{lo}, Error_{la}, and Error_r, indicating that the model proposed in this study exhibits smaller errors in the location and size of segmented craters compared to the real craters. This finding provides evidence for its higher accuracy. Therefore, the embedded encoder–decoder structure in each feature extraction module can strengthen the overall learning capability and multilayer feature extraction ability, to get better performance of crater extraction.

At the same time, we performed a visual comparison, as shown in Fig. 4. The red circles indicate missed craters, the blue circles indicate correctly identified craters, and the green circles indicate new craters. The first row of images indicate that SqUNet network model successfully detects all the craters due to its comprehensive feature extraction capability. In contrast, the other six models have missed some craters. In the second row, it is evident that SqUNet outperforms the other six networks in discovering more new craters. This is mainly attributed to the model's adoption of a deeper network architecture, enabling it to better capture small, blurry, or concealed craters. The third row shows that SqUNet exhibits fewer missed craters. This indicates that the model has a higher recall rate and accuracy. From the fourth row, it can be seen that our network model surpasses

TABLE V
COMPARISON OF DIFFERENT COMPETING MODELS ON LUNAR DEM DATASETS

Metric	DeepMoon	D-LinkNet	ERU-Net	UNet++	NAU-Net	SUNet3+	SqUNet
Recall	78.1%	69.5%	81.3%	74.1%	76.4%	82.7%	**87.5%**
Precision	76.8%	71.7%	72.9%	81.7%	83.1%	82.9%	**80.7%**
F1-score	77.4%	70.6%	76.9%	82.4%	79.6%	82.8%	**82.8%**
F2-score	77.8%	69.9%	79.5%	83.4%	77.7%	82.7%	**85.2%**
$Error_{lo}$	9.3%	11.0%	9.0%	9.5%	9.6%	9.0%	**8.9%**
$Error_{la}$	9.1%	9.2%	7.7%	10.7%	10.0%	8.9%	**8.4%**
$Error_r$	7.5%	9.2%	7.7%	9.6%	8.2%	7.4%	**6.8%**
FPS	29.3	16.7	13.14	18.0	27.0	11.2	**25.9**

The bold values represent the results of each evaluation indicator of SqUNet.

the other six in detecting overlapping or mutually inclusive craters. This is mainly attributed to the enhanced U-shaped encoder–decoder structure for extraction of multilayer features.

D. Generalization Experiment

In order to further verify the generalization ability of SqUNet, we generated a small dataset using Mars DEM images. We utilized the largest and most comprehensive Mars crater catalog database, known as RH2012 [34], as the annotation labels. This catalog comprises statistical data for 384 343 impact craters with diameters exceeding 1 km. For each crater, the catalog includes corresponding latitude, longitude, diameter, and other determinable relevant information. Since Martian craters are primarily distributed within latitude 0°∼60° and longitude −30°∼30°, we created the dataset within this region. The dataset consisted of 3 000 training samples, 300 validation samples, and 300 testing samples. We trained SqUNet on the training dataset for 10 iterations and evaluated its performance on the testing dataset. As shown in Fig. 5, the results demonstrate that SqUNet trained on the small dataset of Mars DEM can identify 87.0% of craters in the testing dataset with an accuracy of 84.8%, and F1-score = 85.9%, F2-score = 86.6%.

To further validate the robustness of our model, we utilized the SqUNet network model to conduct crater detection in three distinct regions on Mars: 1) Longitude (0∼30°), Latitude (0∼30°); 2) Longitude (0-30°), Latitude (−30∼0°); and 3) Longitude (30∼60°), Latitude (−30∼30°). They are part of the Arabia Terra, Noachis Terra, and Sabeaer Terra regions, respectively. We randomly selected 300 DEM images from each region and performed detection using the trained model. The statistical results of all DEM images are presented in Table VI. Our SqUNet model achieved consistent results in the three regions, with precision of 84.0%–84.6% and recall of 85.4%–88.5%. The lower recall rate in the region with longitude 30–60 ° and latitude −30–30° is primarily due to the complex terrain of Sabeaer Terra, which includes numerous mountains and valleys. However, even under these challenging geological conditions, the model still ensures a recall rate of 85.4% for most impact craters. For other regions, both precision and recall exceed 84%, further confirming the effectiveness of our model.
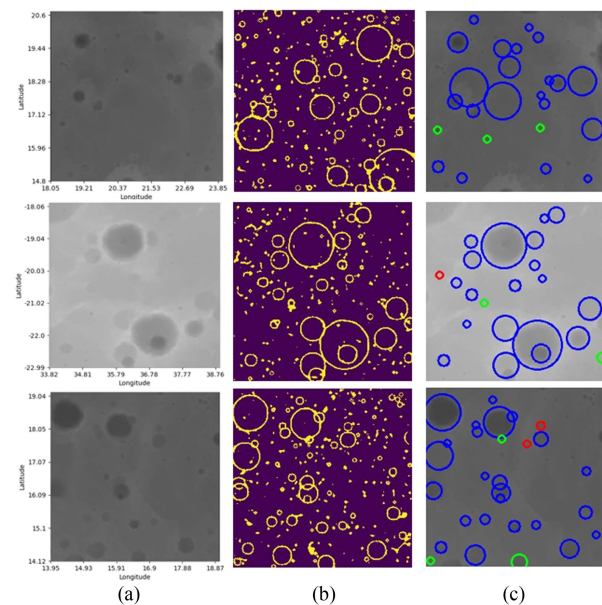

Fig. 5. Crater prediction and extraction results on Mars DEM images (red circles: Missed craters, blue circles: Correctly identified craters, green circles: New craters.). (a) Ground-truth. (b) Segmentation results. (c) Results on SqUNet.

TABLE VI
EVALUATE METRICS OF SQUNET IN FOUR REGIONS

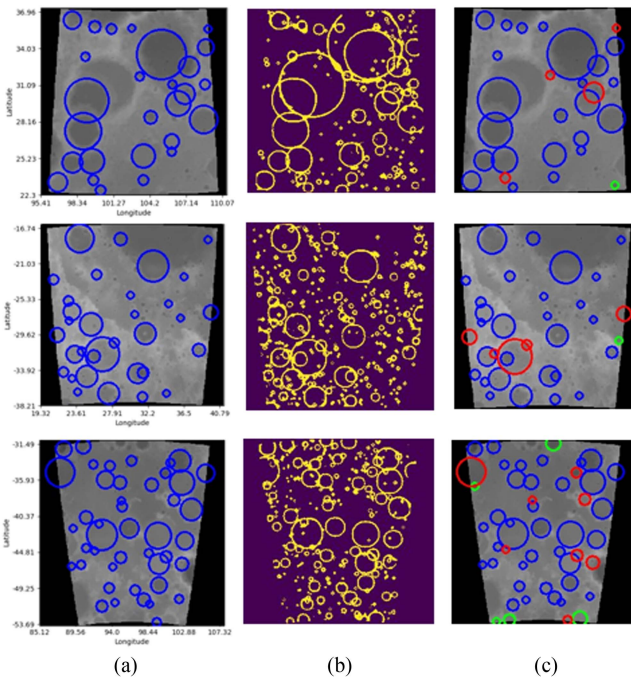| Evaluate metric	lon(0~30) lat(0~30)	lon(0~30) lat(−30~0)	lon(30~60) lat(−30~30)
Recall	86.5%	88.5%	85.4%
Precision	84.0%	84.6%	84.0%
F1-score	76.0%	68.8%	75.5%
F2-score	76.9%	67.7%	78.5%
$Error_{lo}$	6.8%	6.9%	7.1%
$Error_{la}$	6.8%	6.8%	7.1%
$Error_r$	5.7%	5.6%	6.0%

Fig. 6. Crater prediction and extraction results on lunar DEM images (red circles: Missed craters, blue circles: Correctly identified craters, green circles: New craters). (a) Ground-truth. (b) Segmentation results. (c) Results on SqUNet.

IV. DISCUSSION SECTION

In order to perform feature extraction effectively, we explored an embedded U-Net network. Ablation experiments showed that the embedded U-Net module significantly improved the detection performance. We compared the network with the latest four object segmentation methods and confirmed that SqUNet is more suitable for feature extraction of lunar craters. Additionally, we compared our model with six competing models that also used the lunar DEM, and the test results further confirmed the superiority of our network in detection performance, with higher precision and recall rates than the other models. Furthermore, tests on Mars also showed the generalization ability of our model for detecting craters on different planets and its good potential for practical applications.

Although we achieved good results in the design and detection performance of the network model, some problems were still found in the detection results, as shown in Fig. 6, which displays some representative detection results on the lunar DEM test datasets. It can be observed that although most of the craters were successfully identified, there were still small parts of craters missed (indicated by the red circles), and in the segmentation results, the existence of these missed craters can be seen, indicating that a part of the craters was missed during the template matching process, possibly due to too much overlap with adjacent craters resulting in incomplete segmentation results. Therefore, how to improve the template matching algorithm for incomplete segmented crater extraction deserves further investigation.

At present, SqUNet has been able to detect craters to the greatest extent, which can be used as a new basic algorithm for crater detection. But SqUNet only uses a simple convolutional neural network, without combining some powerful feature extraction frameworks, such as: resnet, senet, densenet, and swin transformer. So we believe that the follow-up SqUNet combined with some powerful feature extraction frameworks will have better detection results for some craters with inconspicuous visual features. In addition, the complexity of the SqUNet network model is high and the detection speed is slow, so it is necessary to further improve the network to realize the lightweight and fast network model.

V. CONCLUSION

This article proposes a high-performance crater detection method based on the U-Net. We use an embedded U-Net architecture with an encoding and decoding structure to replace the traditional convolution module. This way, we significantly optimize the feature learning ability. At the same time, we add a skip link inside the embedded U-Net, so that the original feature information can be retained. Our experiments show that the proposed SqUNet is effective and feasible for crater identification from lunar DEM images. Our network achieves better results on different accuracy metrics than other competing models. In addition, the testing results on the Mars DEM dataset have also demonstrated the strong generalization and robustness of the SqUNet network model. This research can help lunar researchers study lunar landform features more efficiently and choose safer landing sites.

In our future work, we will try to migrate the network to other planets, study a high-performance and high-precision model for automatic detection and parameter extraction of craters, and further analyze the characteristics of planetary geomorphology.

REFERENCES

[1] J. W. Head et al., "Global distribution of large lunar craters: Implications for resurfacing and impactor populations," *Science*, vol. 329, pp. 1504–1507, 2010.

[2] B. Wu et al., "Topographic modeling and analysis of the landing site of Chang'E-3 on the Moon," *Earth Planet. Sci. Lett.*, vol. 405, pp. 257–273, Nov. 2014.

[3] B. Wu, J. Huang, and Y. Li, "Rock abundance and crater density in the candidate Chang'e-5 landing region on the Moon," *J. Geophys. Res. Planets*, vol. 123, pp. 3256–3272, 2018.

[4] B. Wu et al., "Landing site selection and characterization of Tianwen-1 (Zhurong rover) on Mars," *J. Geophys. Res., Planets*, vol. 127, 2022, Art. no. e2021JE007.

[5] R. Z. Povilaitis, M. S. Robinson, C. H. van der Bogert, H. Hiesinger, H. M. Meyer, and L. R. Ostrach, "Crater density differences: Exploring regional resurfacing, secondary crater populations, and crater saturation equilibrium on the Moon," *Planet. Space Sci.*, vol. 162, pp. 41–51, 2018.

[6] M. Galloway, J. Paxman, G. Benedix, T. Tan, M. Towner, and P. Bland, "Automated crater detection and counting using the Hough transform and canny edge detection," in *Proc. Workshop Issues Crater Stud. Dating Planet. Surf.*, 2015, Art. no. 9024.

[7] R. Honda, Y. Iijima, and O. Konishi, "Mining of topographic feature from heterogeneous imagery and its application to lunar craters," in *Progress in Discovery Science*. Berlin, Germany: Springer-Verlag, 2002, pp. 395–407.

[8] S. Vijayan, K. Vani, and S. Sanjeevi, "Crater detection, classification and contextual information extraction in lunar images using a novel algorithm," *Icarus*, vol. 226, no. 1, pp. 798–815, 2013.

[9] G. Salamuniccar and S. Loncaric, "Method for crater detection from martian digital topography data using gradient value/orientation, morphometry, vote analysis, slip tuning, and calibration," *IEEE Trans. Geosci. Remote Sens.*, vol. 48, no. 5, pp. 2317–2329, May 2010, doi: 10.1109/TGRS.2009.2037750.

[10] Q. Liu, W. Cheng, G. Yan, Y. Zhao, and J. A. Liu, "Machine learning approach to crater classification from topographic data," *Remote Sens.*, vol. 11, 2019, Art. no. 2594.

[11] M. Chen, D. Liu, K. Qian, J. Li, M. Lei, and Y. Zhou, "Lunar crater detection based on terrain analysis and mathematical morphology methods using digital elevation models," *IEEE Trans. Geosci. Remote Sens.*, vol. 56, no. 7, pp. 3681–3692, Jul. 2018.

[12] A. Silburt et al., "Lunar crater identification via deep learning," *Icarus*, vol. 317, pp. 27–38, 2019.

[13] D. DeLatte, S. Crites, N. Guttenberg, and T. Yairi, "Automated crater detection algorithms from a machine learning perspective in the convolutional neural network era," *Adv. Space Res.*, vol. 64, no. 8, pp. 1615–1162, 2019.

[14] Z. Lichen, C. Zhang, and M. Wu, "D-LinkNet: LinkNet with pretrained encoder and dilated convolution for high resolution satellite imagery road extraction," in *Proc. IEEE/CVF Conf. Comput. Vis. Pattern Recognit. Workshops*, 2018, pp. 192–194.

[15] Y. Li, L. Du, and D. Wei, "Multiscale CNN based on component analysis for SAR ATR," *IEEE Trans. Geosci. Remote Sens.*, vol. 60, 2022, Art. no. 5211212.

[16] E. Shelhamer, J. Long, and T. Darrell, "Fully convolutional networks for semantic segmentation," *IEEE Trans. Pattern Anal. Mach. Intell.*, vol. 39, no. 4, pp. 640–651, Apr. 2017.

[17] O. Ronneberger, P. Fischer, and T. Brox, "U-Net: Convolutional networks for biomedical image segmentation," in *Proc. Int. Conf. Med. Image Comput. Comput.-Assist. Interv.*, 2015, pp. 234–241.

[18] L. C. Chen, Y. Zhu, G. Papandreou, F. Schroff, and H. Adam, "Encoder-decoder with atrous separable convolution for semantic image segmentation," in *Proc. Eur. Conf. Comput. Vis.*, 2018, pp. 801–818.

[19] R. Li et al., "A2-FPN for semantic segmentation of fine-resolution remotely sensed images," *Int. J. Remote Sens.*, vol. 43, no. 3, pp. 1131–1155, 2022.

[20] J. Chen et al., "TransUNet: Transformers make strong encoders for medical image segmentation," 2021, *arXiv:abs/2102.04306*.

[21] H. Cao et al., "Swin-Unet: Unet-like pure transformer for medical image segmentation," *Comput. Vis. ECCV 2022 Workshops*, vol. 13803, pp. 205–218, doi: org/10.1007/978-3-031-25066-8_9.

[22] Z. Liu et al., "Swin transformer: Hierarchical vision transformer using shifted windows," in *Proc. IEEE/CVF Int. Conf. Comput. Vis.*, 2021, pp. 9992–10002, doi: 10.1109/ICCV48922.2021.00986.

[23] C. Lee, "Automated crater detection on Mars using deep learning," *Planet. Space Sci.*, vol. 170, pp. 16–28, 2019.

[24] S. Wang, Z. Fan, Z. Li, H. Zhang, and C. Wei, "An effective lunar crater recognition algorithm based on convolutional neural network," *Remote Sens.*, vol. 12, 2020, Art. no. 2694.

[25] Y. Mao, R. Yuan, W. Li, and Y. Liu, "Coupling complementary strategy to U-Net based convolution neural network for detecting lunar impact craters," *Remote Sens.*, vol. 14, no. 3, 2022, Art. no. 661, doi: 10.3390/rs14030661.

[26] Y. Jia, L. Liu, and C. Zhang, "Moon impact crater detection using nested attention mechanism based UNet++," *IEEE Access*, vol. 9, pp. 44107–44116, 2021, doi: 10.1109/ACCESS.2021.3066445.

[27] Y. Wu, G. Wan, L. Liu, Y. Jia, Z. Wei, and S. Wang, "Fast and accurate crater detection on martian surface using S/UN et 3+," in *Proc. IEEE 6th Inf. Technol. Mechatron. Eng. Conf.*, 2022, pp. 683–687, doi: 10.1109/ITOEC53115.2022.9734410.

[28] LRO LOLA and Kaguya Terrain Camera DEM, [Online]. Available: https://zenodo.org/record/1133969

[29] "Catalog of two lunar crater datasets," [Online]. Available: https://github.com/silburt/DeepMoon/tree/master/catalogues

[30] U.K. Met Office, "Cartopy: A cartographic Python library with a matplotlib interface," 2015. Accessed: Mar. 15, 2019. [Online]. Available: http://scitools.org.uk/cartopy/index.html

[31] S. Van der Walt et al., "Scikit-image: Image processing in Python," *PeerJ*, vol. 2, 2014, Art. no. e453.

[32] N. Ketkar and J. Moolayil, "Introduction to pytorch," in *Deep Learning With Python*. Berlin, Germany: Springer-Verlag, 2021, pp. 27–91.

[33] Z. Zhou, M. M. R. Siddiquee, N. Tajbakhsh, and J. Liang, "UNet++: Redesigning skip connections to exploit multiscale features in image segmentation," *IEEE Trans. Med. Imag.*, vol. 39, no. 6, pp. 1856–1867, Jun. 2020, doi: 10.1109/TMI.2019.2959609.

[34] S. J. Robbins and B. M. Hynek, "A new global database of Mars impact craters ≥ 1 km: 1. Database creation, properties, and parameters," *J. Geophys. Res. Planets*, vol. 117, 2012, Art. no. 2011JE003966.

Yaqi Zhao received the B.E. degree (Hons.) in communication engineering from Zhengzhou University, Zhengzhou, China, in 2021. She is currently working toward the M.S. degree with the School of Information Science and Technology in Fudan University, Shanghai, China.

Her current research interests include planetary target recognition and planetary topography.

Hongxia Ye (Senior Member, IEEE) received the M.S. degree in electromagnetic theory and computational electromagnetics from Xi'an Jiaotong University, Xi'an, China, in 2003, and the Ph.D. degree in electromagnetic wave scattering and remote sensing from Fudan University, Shanghai, China, in 2007.

She is currently an Associate Professor with the School of Information Science and Engineering, Fudan University. She has authored more than 70 articles and a book. Her research interests include wave propagation and scattering, SAR imaging simulation, and planetary remote sensing.